

Direct and inverse solver for the 3D optoacoustic Volterra equation

J Stritzel, O Melchert, M Wollweber and B Roth

Hannover Centre for Optical Technologies (HOT), Leibniz Universität Hannover,
Nienburger Str. 17, D-30167 Hannover, Germany

E-mail: jenny.stritzel@hot.uni-hannover.de

Abstract. The *direct problem* of optoacoustic signal generation in biological media consists of solving the inhomogeneous optoacoustic wave equation for an initial acoustic stress profile. In contrast, the mathematically challenging *inverse problem* requires the reconstruction of the initial stress profile from a proper set of observed signals.

In this article, we consider the particular case of a Gaussian transverse irradiation source profile in the paraxial approximation of the wave equation, for which the direct problem along the beam axis can be cast into a linear Volterra integral equation of the second kind. This integral equation can be used in two ways: as a *forward solver* to predict optoacoustic signals in terms of the direct problem, and as an *inverse solver* for which we here devise highly efficient numerical schemes used for the reconstruction of initial pressure profiles from observed signals, constituting a methodical progress of computational aspects of optoacoustics.

In this regard, we explore the validity as well as the limits of the inversion scheme via numerical experiments, with parameters geared towards actual optoacoustic problem instances. The considered inversion input consists of *synthetic* data, obtained by means of forward solvers based on the Volterra integral, and, more generally, the optoacoustic Poisson integral. Regarding the latter, we numerically invert signals that correspond to different detector-to-sample distances and assess the convergence to the true initial stress profiles upon approaching the far-field. Finally, we also address the effect of noise on the quality of the reconstructed pressure profiles.

PACS numbers: 02.30.Zz, 02.60.Nm, 78.20.Pa

Keywords: Optoacoustics, Volterra integral equation, direct solver, inverse solver

1. Introduction

The *inverse* optoacoustic (OA) source reconstruction problem is concerned with the recovery of initial acoustic stress profiles from measured OA signals upon knowledge of the mathematical model that mediates the underlying diffraction transformation [1, 2, 3]. It is the conceptual analogue of the *direct* OA problem (known as the OA *forward* problem), representing the calculation of a diffraction-transformed acoustic pressure

signal at a given field point for a given initial acoustic stress profile on the basis of the OA wave equation [2, 3, 4, 5].

During the last decades, the former problem has received much attention within the field of optoacoustics, owing to its immediate relevance for medical applications, see, e.g., Refs. [6, 7], that aim at the reconstructions of “internal” OA material properties from “external” measurements. In this regard, current progress is mostly due to photoacoustic tomography (PAT) and imaging applications supporting different approaches that might be divided into three groups: (i) back-projection approaches in time or frequency domain [8, 9], (ii) time-reverse evolution of the linear (“T-symmetric”) OA wave equation [10, 11], (iii) model-based least-squares schemes [12, 13], also involving more hybrid approaches, based, e.g., on the ideas of image reconstruction via compressed sensing [14] or Landweber iteration schemes [15]. All these approaches are equipped with their own benefits and drawbacks. In particular, note that the inversion input for PAT backpropagation approaches consists of a multitude of signals recorded on a surface enclosing the OA source volume. In contrast, we here introduce an alternate approach that allows for the numerical reconstruction of initial stress profiles via inversion of signals from “single-shot” measurements. Therefore we focus on the direct and inverse problem in the paraxial approximation to the full OA wave equation [16, 4], where we allude to a numerical treatment of an underlying integral equation, capturing the diffraction-transformation of signals for an on-axis setting, leading to highly efficient forward and inverse solvers for the OA problem in the considered setting.

After developing and testing the numerical procedure, we assess how well the particular source reconstruction problem performs beyond the paraxial approximation by considering: (i) signals obtained for the full OA wave-equation in the acoustic far-field, and, (ii) synthetic signals exhibiting noise. To the knowledge of the authors, within the field of optoacoustics no such numerical procedure has been discussed and put under scrutiny, yet. Hence, we present a methodical progress in the field of optoacoustics, appealing from the point of view of computational theoretical physics.

The remainder of the article is organized as follows. In section 2, we briefly summarize the theoretical background of OA signal generation and calculation. In section 3 we elaborate on our numerical approaches that yield forward and inverse solvers for the OA problem in the paraxial approximation, followed by a sequence of numerical experiments described in section 4. We summarize and conclude upon our findings in section 5.

2. Theoretical aspects of optoacoustic (OA) signal generation

In the subsequent subsections we briefly review the theoretical foundation of the mechanism of optoacoustic signal generation. In this regard, in subsection 2.1, we first detail a forward solution of the general problem based on the *OA Poisson integral*. After this, in subsection 2.2, we allude to a particular “on-axis” variant of the forward problem, paving the way for a highly efficient inversion scheme in terms of an *OA*

Volterra integral.

2.1. General optoacoustic signal generation – The OA Poisson integral

Albeit there are several microscopic mechanisms that possibly contribute to the generation of optoacoustic signals [17], we restrict the subsequent theoretical discussion to the most dominant photothermal heating effect, i.e. thermal expansion. Further, we consider a pulsed optoacoustic working mode with a pulse duration that is: (i) significantly smaller than the thermal relaxation time of the surrounding material [18, 19], realizing what is referred to as *thermal confinement*, and, (ii) short enough to be represented by a delta-function on the scale of typical acoustic propagation times [20], denoted by *stress confinement*.

Then, focusing on the acoustic aftermath of the thermoelastic expansion mechanism, the scalar excess pressure field $p(\vec{r}, t)$ at time t and field point \vec{r} can be related to an initial stress distribution $p_0(\vec{r})$ via the inhomogeneous optoacoustic wave equation [2, 17]

$$[\partial_t^2 - c^2 \vec{\nabla}^2] p(\vec{r}, t) = \partial_t p_0(\vec{r}) \delta(t), \quad (1)$$

wherein c signifies the speed of sound and where the initial stress field is related to the volumetric energy density $W(\vec{r})$ [2, 21], deposited in the irradiated region via absorption and photothermal heating by the short laser pulse, according to $p_0(\vec{r}) = \Gamma W(\vec{r})$. Therein, Γ refers to the Grüneisen parameter, an effective parameter describing the fraction of absorbed heat that is actually converted to mechanical stress. Note that in Eq. (1), temporal changes of the local photothermal heat absorption field $W(\vec{r})\delta(t)$ trigger stress waves that propagate through the medium and constitute the optoacoustic signal.

An analytic solution that yields the excess pressure $p(\vec{r}, t)$ according to Eq. (1) is accessible through the corresponding Greens-function in free space, establishing the optoacoustic Poisson integral [5, 2, 18]

$$p(\vec{r}, t) = \frac{1}{4\pi c} \partial_t \int_V \frac{p_0(\hat{r})}{|\vec{r} - \hat{r}|} \delta(|\vec{r} - \hat{r}| - ct) d\hat{r}, \quad (2)$$

wherein V represents the “source volume” beyond which the initial stress $p_0(\vec{r}) = 0$ [22], and $\delta(\cdot)$ limiting the integration to a time-dependent surface centered at \vec{r} and radially constrained by $|\vec{r} - \hat{r}| = ct$.

2.2. Diffraction transformation in the paraxial approximation – The OA Volterra integral equation

In the remainder of the article we consider non-scattering compounds which consist of plane-parallel layers, stacked along the z -direction of an associated coordinate system within the positive half space. The acoustic properties within the bulk are assumed to be constant, whereas the optical properties are set to be constant within the layers but

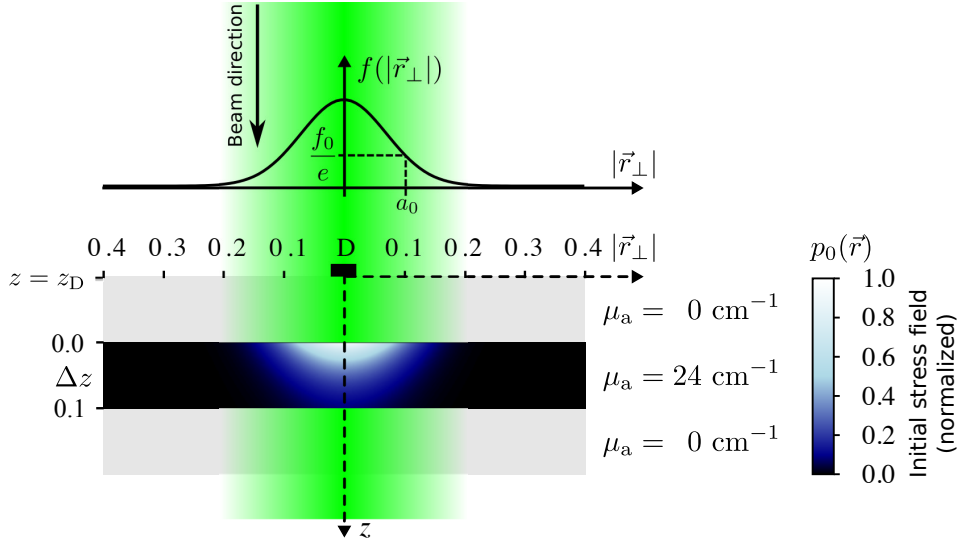


Figure 1. (Color online) Illustration of an optoacoustic setup with plane-normal irradiation source profile $f(|\vec{r}_\perp|)$ and a source volume consisting of possibly multiple stacked absorbing layers. The irradiation source exhibits a $1/e$ -intensity radius of $|\vec{r}_\perp| = a_0$ and the different layers possess absorption coefficients μ_a as indicated in the figure. Here, the figure shows a single absorbing layer of width $\Delta z = 0.1$ cm. The initial stress field $\propto p_0(\vec{r})$ causes acoustic pressure waves that can be monitored as an optoacoustic signal at the detection point D, here located on the beam axis, i.e. at $|\vec{r}_\perp| = 0$, with distance $z_D < 0$ from the absorbing layer.

may differ from layer to layer, characterized by a depth-dependent absorption coefficient $\mu_a(\vec{r}) \equiv \mu_a(z)$, see Fig. 1. Then, for an inherently 2D plane-normal irradiation source profile $f(\vec{r}_\perp)$, the initial stress field can be factored according to

$$p_0(\vec{r}) = \Gamma f(\vec{r}_\perp) g(z), \quad (3)$$

wherein $g(z)$ summarizes the effect of the absorptive properties of the layered medium in terms of a 1D axial absorption depth profile. Bearing in mind that we consider non-scattering media, the latter follows Beer-Lamberts law, i.e.

$$g(z) = \mu_a(z) \exp \left\{ - \int_0^z \mu_a(z') dz' \right\}. \quad (4)$$

Note that such a factorization of $p_0(\vec{r})$ is well justified: there are numerous studies where experiments and their complementing simulations are in accord with the above constraints, see, e.g., Refs. [23, 24, 21, 25, 26].

Further, let $f(\vec{r}_\perp)$ be an axially symmetric irradiation source profile with a Gaussian transverse profile, i.e.

$$f(\vec{r}_\perp) = f_0 \exp \left\{ - |\vec{r}_\perp|^2 / a_0^2 \right\}, \quad (5)$$

wherein f_0 signifies the incident radiant exposure on the beam axis $|\vec{r}_\perp| = 0$ and a_0 defines the $1/e$ -threshold of the beam intensity. This is a realistic assumption for many excitation sources applied in OA.

Under the above prerequisites, it can be shown that the diffraction transformation of laser-excited excess pressure profiles in the paraxial approximation of Eq. (1) at a detection point \vec{r}_D along the beam axis, i.e. $p_D(\tau) \equiv p(\vec{r}_D, t)|_{(\vec{r}_\perp=0, \tau=t+z_D/c)}$, can properly be described in terms of a Volterra integral equation of the 2nd kind [4, 16, 27], here referred to as the *optoacoustic Volterra integral*, reading

$$p_D(\tau) = p_0(\tau) - \int_{-\infty}^{\tau} \mathcal{K}(t, \tau) p_0(t) dt. \quad (6)$$

In the above, the change of argument in the description of the initial stress has to be understood as $p_0(\tau) = p_0(\vec{r})|_{(\vec{r}_\perp=0, \tau=t+z_D/c)}$. The Volterra operator, i.e. the second term in the equation above, describes the diffraction transformation experienced by the OA signal. It governs the propagation of acoustic stress waves in the optoacoustic on-axis setting with Gaussian irradiation source profile via a convolution type Volterra kernel $\mathcal{K}(t, \tau) = \mathcal{K}(\tau - t)$, wherein [16]

$$\mathcal{K}(\tau - t) = \omega_D \exp \{ -\omega_D (\tau - t) \}. \quad (7)$$

Therein $\omega_D = 2c|z_D|/a_0^2$ denotes a characteristic OA frequency, related to the two “exterior” OA lengthscales given by: (i) the distance $|z_D|$ between detection point and absorbing layer, and, (ii) the transversal characteristic lengthscale a_0 of the irradiation source profile. The dependence of the diffraction transformation on the frequencies ω_D and $\omega_a = \mu_a c$, the latter signifying the characteristic frequency of the OA signal spectrum, is detailed in the literature, see, e.g., Ref. [16]. Note that in response to z_D and a_0 , the frequency ω_D is either decreasing or increasing, defining the acoustic near-field (NF) and far-field (FF) from the value of the associated dimensionless diffraction parameter

$$D = \omega_D/\omega_a \quad (8)$$

in the regimes $D < 1$ and $D > 1$, respectively.

Note that the OA Volterra integral Eq. (6) not only allows to solve the OA forward problem, i.e. the calculation of the excess pressure $p(z_D, \tau)$ given $p_0(\tau)$ and $\mathcal{K}(\tau, t)$, but also keeps the possibility to solve the inverse OA source problem, i.e. the reconstruction of $p_0(\tau)$ given $p(z_D, \tau)$ and $\mathcal{K}(\tau, t)$, as will be detailed in the section below.

3. Numerical implementation of the OA forward and inverse solvers

We will now elaborate on the numerical approaches we ensued in order to solve the OA forward and inverse problems, see subsections 3.1 and 3.2, respectively. In doing so we also emphasize some important implications the special case of a Gaussian transverse irradiation source profile has on our numerical implementation.

3.1. Forward solution

Regarding the solution process of the “direct” OA problem, i.e. the calculation of $p_D(\tau)$ for a given distribution of initial acoustic stress $p_0(\tau)$, we follow two distinct approaches.

In subsection 3.1.1, we first introduce a forward solver based on a numeric solution of the OA Poisson integral Eq. (2), followed by a more model-tailored solver based on a forward solution of the OA Volterra integral Eq. (6). For completeness, while the optoacoustic Volterra equation can be used for both, the calculation of $p_D(\tau)$ as well as for the reconstruction of $p_0(\tau)$, we will subsequently need the Poisson integral based solver for benchmarking and generation of synthetic OA signals that serve as input for the inversion procedure. This is necessary in order to formally de-couple the forward solution and inversion processes.

3.1.1. Forward solver based on the OA Poisson integral: Here, we opt for an implementation of Eq. (2) for layered media in cylindrical polar coordinates. The respective implementation is available as “SONOS – a fast poisson integral solver for layered homogeneous media” [28], and, albeit being restricted to a solely z -dependent absorption coefficient, it allows for the efficient calculation of OA signals resulting from general irradiation source profiles with an axial symmetry at arbitrary detection points $\vec{r}_D = (\rho_D, z_D)$. Therein, z_D signifies the axial coordinate of the detection point in the reference frame in which the nearest absorbing layer has $z = 0$, see Fig. 1, and ρ_D denotes the deviation of the detection point from the symmetry axis of the beam profile. Here, since we are only interested in the calculation of OA signals along the beam axis ($\rho_D = 0$), we can further simplify the numerical procedure detailed in Ref. [26] to some extent. Since the on-axis view of the irradiation source profile in the detection-point based reference frame is independent of the azimuthal angle, and therefore $f_D(\rho) = f_0 \exp\{-\rho^2/a_0^2\}$, the respective integration in a cylindrical polar representation of Eq. (2) can be carried out explicitly, resulting in the simplified expression

$$p_D(t) = \frac{\Gamma}{2c} \partial_t \int_{\rho} \int_z \rho \frac{f_D(\rho) g_D(z)}{(\rho^2 + z^2)^{1/2}} \delta((\rho^2 + z^2)^{1/2} - ct) d\rho dz. \quad (9)$$

Note that in the above equation, the distance z is to be measured with respect to the detection point D, with the nearest absorbing layer located at $z = |z_D|$. Further, the δ -distribution might be interpreted as an indicator function that bins the values of the integrand according to the propagation time of the respective stress waves. This already yields a quite efficient numerical scheme to compute the OA signal $p_D(t)$ at the detection point, since the pending integrations can, in a discretized setting where $\rho_i = i\Delta_\rho$, $i = 0, \dots, N_\rho$, and $\Delta_\rho = \rho_{\max}/N_\rho$ as well as $z_i = |z_D| + i\Delta_z$, $i = 0, \dots, N_z$, and $\Delta_z = (z_{\max} - |z_D|)/N_z$, be carried out with time complexity of order $O(N_\rho N_z)$. During our numerical experiments, since we are only interested in the general shape of the optoacoustic signal, we set the value of the constants in Eq. (9) to $\Gamma/c \equiv 2/f_0$. Thus, the resulting OA signal is obtained in arbitrary units, subsequently abbreviated as [a.u.]. Finally, so as to mimic the finite thickness Δw of the transducer foil in an experimental setup [26], we grant the option to average $p_D(t)$ at the detection point over a time interval $\Delta t = \Delta w/c$.

3.1.2. Forward solver based on the OA Volterra integral: While there exist standard procedures for the numerical (forward) solution of Volterra integral equations of the 2nd kind, e.g. based on an approximation of the diffraction term in Eq. (6) in terms of a trapezoidal rule [29] (or other quadrature rules [30], for that matter), we can simplify the approach for a general kernel $\mathcal{K}(\tau, t)$ by capitalizing on the special form of the OA stress wave propagator. Since the latter is of convolution type, i.e. $\mathcal{K}(\tau, t) \equiv \mathcal{K}(\tau - t) = \omega_D \exp\{-\omega_D(\tau - t)\}$, Eq. (6) can be solved for $p_D(\tau)$ via memoization [31]. Therefore, and with regard to the upcoming inversion step in subsection 3.2.1, it is beneficial to put the diffraction term in Eq. (6) under scrutiny. As it turns out, in a discretized setting where $t_i = i\Delta_t$, $i = 0, \dots, N$, $\Delta_t = t_{\max}/N$, and thus $\tau_i = t_i + z_D/c$, abbreviating $\mathcal{K}(\tau_i - \tau_j)$ and $p_0(\tau_i)$ as $\mathcal{K}_{i,j}$ and $p_{0,i}$, respectively, we have $\mathcal{K}_{i,i} = \omega_D$ and $\mathcal{K}_{i+2,i} = \mathcal{K}_{i+1,i} \exp\{-\omega_D\Delta_t\}$, yielding a recurrence relation that approximates the diffraction term according to

$$\begin{aligned} I_i &= \int_{\tau_0}^{\tau_i} \mathcal{K}(\tau_i - t') p_0(t') dt' \\ &= \left[\mathcal{K}_{i,0} p_{0,0} + 2 \sum_{j=1}^{i-1} \mathcal{K}_{i,j} p_{0,j} + \mathcal{K}_{i,i} p_{0,i} \right] \Delta_t / 2 \\ &= I_{i-1} \exp\{-\omega_D\Delta_t\} + (\omega_D\Delta_t/2) \left[p_{0,i-1} \exp\{-\omega_D\Delta_t\} + p_{0,i} \right]. \end{aligned} \quad (10)$$

In the above expression the trapezoidal approximation becomes exact in the limit $N \rightarrow \infty$. Consequently, the OA signal $p_{D,i} \equiv p_D(\tau_i)$ can be obtained by simply marching in time, i.e.

$$p_{D,i} = p_{0,i} - I_i, \quad (i = 1, \dots, N) \quad (11)$$

starting off at $p_{D,0} = p_{0,0}$, $I_0 = 0$ and updating I_i via Eq. (10).

Note that adopting a standard discretized scheme for the calculation of $p_D(\tau)$, set up for a general kernel $\mathcal{K}(\tau, t)$ [29], would yield an algorithm that terminates in time $O(N^2)$ since the full integral has to be re-computed at each time-step due to the “wandering” upper bound. Note that this would not mean much an improvement over the full wave equation solver discussed in subsection 3.1.1 as one has $N \approx N_z$. However, since the OA stress wave propagator is actually of convolution type and can be decomposed into a product of exponential factors at each time-step, we here yield a highly efficient custom forward solver with time complexity $O(N)$.

3.2. Inverse solution

We can accomplish the highly non-trivial task of solving the inverse OA source problem, i.e. the reconstruction of $p_0(\tau)$ given $p_D(\tau)$ and $\mathcal{K}(\tau, t)$ via Eq. (6), in basically two ways: by means of (i) an inversion scheme that complements the Volterra integral based forward solver presented earlier, see subsection 3.2.1, and, (ii) an independent algorithmic procedure based on the idea of iteratively improving a putative initial solution, see subsection 3.2.2.

3.2.1. Inverse solver based on the OA Volterra integral: In terms of the recurrence relation approach that yields the diffraction term in Eq. (6) at time-step i via memoization, see Eq. (10), the actual inversion step is only slightly more involved than the forward solution. I.e., the inverse solution in terms of the OA Volterra integral equation can be accomplished by updating the values of $p_{D,i}$ and I_i in a leap-frog manner according to

$$\begin{aligned} p_{0,i} &= \left(1 - \omega_D \Delta_t / 2\right)^{-1} \left[p_{D,i} + \left(I_{i-1} + (\omega_D \Delta_t / 2) p_{0,i-1} \right) \exp\{-\omega_D \Delta_t\} \right] \quad (12) \\ I_i &= I_{i-1} \exp\{-\omega_D \Delta_t\} + (\omega_D \Delta_t / 2) \left[p_{0,i-1} \exp\{-\omega_D \Delta_t\} + p_{0,i} \right], \end{aligned}$$

starting off at $p_{0,0} = p_{D,0}$ and $I_0 = 0$. Thus, the numerical expense of the Volterra integral based inverse solver amounts to only $O(N)$.

Far-field inversion – Considering a far-field (FF) setup wherein the distance between the detection point D and the absorbing layers is large, i.e. $z_D \rightarrow \infty$ and the width of the irradiation source profile is narrow enough to ensure a diffraction parameter $D \gg 1$ (also referred to as Fraunhofer zone [32]; a parameter region also important for approximate OA imaging methods [11, 33]), the OA signal $p_{D,FF}(\tau)$ is related to the initial OA stress profile $p_0(\tau)$ via [16, 21]

$$p_{D,FF}(\tau) = \frac{1}{\omega_D} \frac{d}{d\tau} p_0(\tau). \quad (13)$$

Thus, in the far-field approximation the initial stress profile $p_{0,FF}(\tau)$ can be obtained by numerical quadrature using the above equation.

3.2.2. Inverse solver based on successive approximations: For numerical redundancy and so as to establish a broad computational foundation for the Volterra integral based approach to inverse optoacoustics, we employed a further, independent reconstruction scheme. It relies on the continued refinement of a putative solution in terms of the Picard-Lindelöf iteration method [34], wherein a properly guessed first approximation $p_0^{(0)}(\tau)$ of $p_0(\tau)$ is improved successively by solving

$$p_0^{(n+1)}(\tau) = p_D(\tau) + \int_{-\infty}^{\tau} \mathcal{K}(\tau - t) p_0^{(n)}(t) dt. \quad (14)$$

I.e. the overall numerical effort to advance from approximation $n \rightarrow n + 1$ in the above correction procedure amounts to a numerical integration that can be accomplished in a time linear in the number of interpolation steps. On very general grounds, the Chebyshev-norm of the difference between two successive solutions $c_n \equiv \|p^{(n+1)}(\tau) - p_0^{(n)}(\tau)\|$ becomes arbitrarily small as $n \rightarrow \infty$ and $p_0(\tau) = \lim_{n \rightarrow \infty} p_0^{(n)}(\tau)$. From a practical point of view we terminated the iteration scheme as soon as the above norm decreases below the threshold $c_n \leq 10^{-6}$, observing that the procedure converges quite fast, i.e. within $O(10 - 60)$ approximation cycles, see the discussion in section 4.3. Note that thus, the time complexity of the solver is basically limited by the time spent for the repeated computation of the integrating

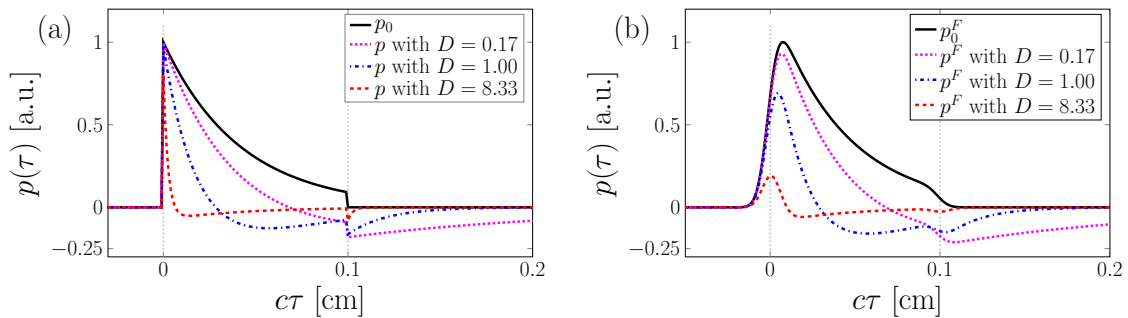


Figure 2. (Color online) Forward calculation of optoacoustic signals $p(\tau)$ in the framework of the Volterra integral equation. In either subfigure, p_0 (black solid lines) indicates the on-axis profile of the initial stress according to Eqs. (3-5). The figures illustrate the change in shape of the optoacoustic signals as perceived at detection points with increasing detector-to-layer distance $z_D = -0.02$ cm (magenta dotted line), -0.1 cm (blue dash-dotted line), -1 cm (red dashed line), characterized by the diffraction parameters $D = 0.17, 1.0, \text{ and } 8.33$, respectively. (a) forward solution of a “genuine”, i.e. non-preprocessed initial stress profile p_0 , (b) forward solution of an $\Delta_z = 0.01$ cm sliding average Gaussian smoothed initial stress profile.

term. For a proper choice of a “predictor” $p_0^{(0)}(\tau)$ one might distinguish two main reconstruction regimes:

Near-field reconstruction – As a high-precision predictor we here use the initial guess $p_0^{(0)}(\tau) \equiv p(z_D, \tau)$ since we can expect the OA near-field signal to be still quite close to the distribution of initial stress $p_0(\tau)$. In contrast to this, a low-precision predictor can be obtained by setting $p_0^{(0)}(\tau) \equiv p_0$, where e.g. $p_0 = 1$.

Far-field reconstruction – As a high-precision predictor we might use the initial guess $p_0^{(0)}(\tau) \equiv p_{0,\text{FF}}(\tau)$, obtained by integrating the OA signal $p(z_D, \tau)$ in the far-field approximation Eq. (13). In opposition to this, a low-precision predictor can be obtained by again setting $p_0^{(0)}(\tau) \equiv p_0$.

4. Numerical experiments

The simulation parameters used for the subsequent numerical experiments are geared towards actual “laboratory” parameters for existing polyvinyl alcohol hydrogel (PVA-H) based tissue phantoms used in the combined experimental and numerical study reported in Ref. [26]. These consist of melanin doped absorbing layers in between two layers of clear PVA-H, quite similar to the setup illustrated in Fig. 1. Here, we assume that the PVA-H layers are non-absorbing and that the melanin doped layer exhibits an absorption coefficient of $\mu_a = 24 \text{ cm}^{-1}$. Albeit the irradiation source profile in such an experimental setting is usually assumed to be of “top-hat” type [21, 24, 26] (e.g. Ref. [26] report an overall $1/e$ radius of approximately 1.2 cm), we here assume an effective Gaussian beam profile with $1/e$ radius $a_0 = 0.1$ cm. This stimulating light beam meets

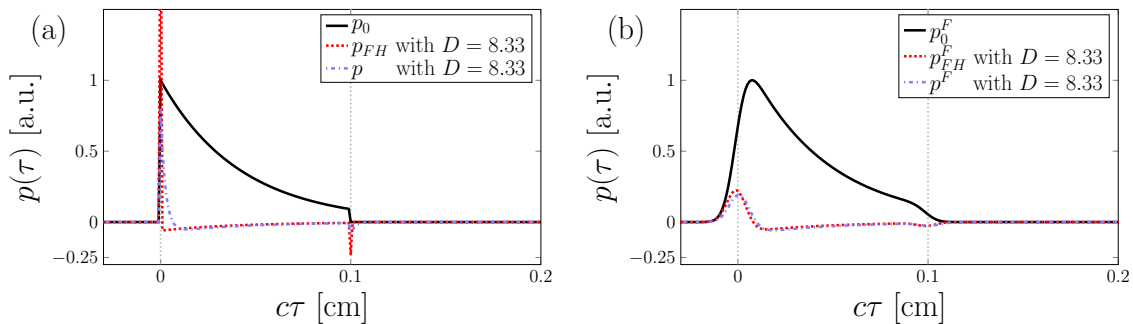


Figure 3. (Color online) Forward calculation of optoacoustic signals in a far-field approximation considering Eq. (13). In either subfigure, p_0 (black solid lines) indicates the on-axis profile of the initial acoustic stress. The figures illustrate the difference in the approximate FF formula, resulting in the signal p_{FH} (red dashed curve), relative to the exact solution p (red dash-dotted curve) at $z_D = -1$ cm, i.e. $D = 8.33$. (a) forward solution of a “genuine”, i.e. non-preprocessed initial stress profile p_0 , (b) forward solution of a smoothed initial stress profile ($\Delta_z = 0.01$ cm sliding average Gaussian smooth).

the absorbing layer at $z = 0$ and leaves it at $z = \Delta z$. The resultant acoustic signal is computed for a field point located along the beam axis at position $z = z_D < 0$.

4.1. Forward and inverse solution within the OA Volterra framework

In the first series of numerical experiments, we deliberately stayed within the framework of the paraxial approximation [35], i.e. we accomplished the forward and inverse calculations by means of the solvers derived from the optoacoustic Volterra equation. Such an approach might be considered as committing inverse crime [36], i.e. performing a (putative) trivial inversion of synthetic data obtained by first solving the forward problem in terms of the same exact model. However, here we use this approach as a proof of principle and consider an independent forward solver (with no connection to the Volterra based solver) in subsequent sections. Albeit there is a wealth of literature discussing OA signals and their change in shape upon advancing from a measurement point located in the acoustic near-field (NF) to a point in the far-field (FF), see e.g. Refs. [4, 16, 32], we first aimed at briefly illustrating the respective diffraction triggered signal changes for our particular single-layer setup by considering different values of z_D .

Solving the direct problem – In this regard, Fig. 2 illustrates the forward calculation of OA signals in a discretized setting, where $z_i = z_{\min} + i\Delta_z$, $i = 1, \dots, N$, and $\Delta_z = (z_{\max} - z_{\min})/N$, starting from an absorption profile obtained using Eqs. (3) and (4), i.e. following Beer-Lamberts law for pure absorbers. Here, we used $z_{\min} = 0.0$ cm, $z_{\max} = 0.1$ cm, $N = 300$ as well as $c = 1$, thus $\tau_i = z_i$. While Fig. 2(a) relates to the forward solution of the OA problem for a non-preprocessed distribution of initial stress, Fig. 2(b) refers to a smoothed initial condition where p_0 is preprocessed using a $\Delta_z = 0.01$ cm sliding average Gaussian filter to mimic a laboratory scenario wherein

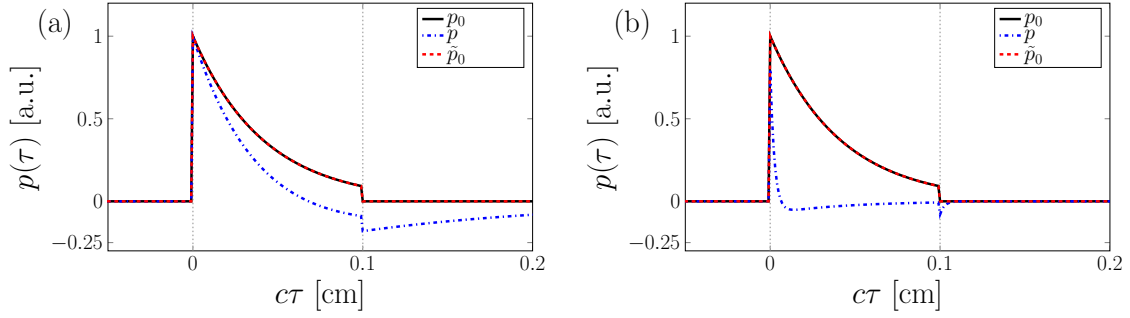


Figure 4. (Color online) Reconstruction of the initial acoustic stress \tilde{p}_0 from computed OA signals p upon knowledge of the diffraction propagator \mathcal{K} in (a) the acoustic NF at $z_D = -0.02$ cm, i.e. $D = 0.17$, and (b) the acoustic FF at $z_D = -1.0$ cm, i.e. $D = 8.33$. The OA source reconstruction is accomplished with the leap-frog algorithm introduced in subsect. 3.2.1. In either case, the reconstructed stress profiles perfectly match the true initial stress profiles p_0 .

the increase and decrease in absorption coefficient is less sudden. Note that the general shape of the OA NF signal, characterized by the diffraction parameter $D = 0.17$, is still strongly reminiscent of the shape of the absorption profile. However, the initial compression phase has already noticeably transformed by diffraction, giving rise to an extended rarefaction phase above a retarded signal depth of ≈ 0.08 cm, extending well beyond the signal depth that characterized the end of the absorbing layer. In contrast to this, the borderline FF ($D = 1.0$) and FF ($D = 8.33$) signals allow for a proper OA depth profiling: both feature a pronounced compression peak that signals an increase of the absorption coefficient μ_a at $z = 0$ cm, followed by an extended rarefaction phase until a sharp (in case of Fig. 2(a); smooth cusp in case of Fig. 2(b)) rarefaction dip signals a sudden decrease of the absorption coefficient at $z = 0.1$ cm continued by a further rarefaction phase rapidly decaying in amplitude. Note that Fig. 2(b) boldly reveals a particular property of OA FF signals: since in the acoustic FF $p(\tau)$ is related to $p_0(\tau)$ via differentiation, see Eq. (13), the peak value of the initial compression phase shifts towards the inclination point of the leading edge of $p_0(\tau)$ as D increases. As evident from Fig. 3, the simplified calculation of the OA signal in the FF approximation according to Eq. (13) is already quite precise at $D = 8.33$, improving further in quality as $|z_D| \rightarrow \infty$ (not shown). Albeit there is still a slight difference between the FF signal estimator $p_{\text{FF}}(\tau)$ and the exact signal shape $p(\tau)$ for the genuine distribution of initial stress (see Fig. 3(a)), the difference seems less pronounced in case of the smoothed initial stress configuration shown in Fig. 3(b).

Solving the inverse OA source reconstruction problem – In a second set of numerical experiments we aimed at solving the inverse optoacoustic problem, where the aim is to reconstruct the initial distribution of acoustic stress p_0 from the measured signal p upon knowledge of the optoacoustic stress propagator \mathcal{K} . As evident from Fig. 4, the Volterra Integral equation based inverse solver outlined in subsection 3.2.1 accomplishes

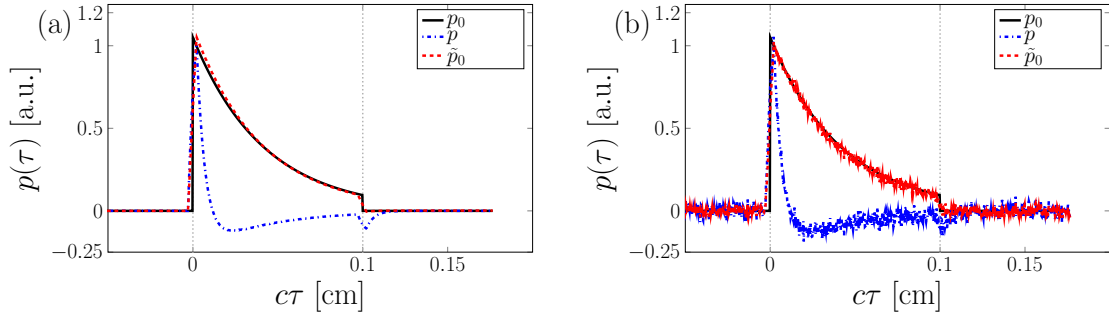


Figure 5. (Color online) Solution of the source reconstruction problem using the Volterra integral equation based inverse solver. The figure illustrates the reconstruction of the initial acoustic stress profile \tilde{p}_0 (dashed red line) from a far-field signal p (dash-dotted blue line), calculated at $z_D = -1$ cm. The true initial stress profile is given by p_0 (solid black line). (a) reconstruction starting from a genuine, i.e. non-postprocessed OA signal p . (b) reconstruction in presence of noise. To obtain the noisy signal, the genuine OA signal was superimposed by Gaussian white-noise with a signal-to-noise ratio of 5.

this task in efficient fashion: irrespective of whether the inversion is performed in the acoustic NF or FF, see Figs. 4(a) and (b), respectively, the reconstructed stress profiles \tilde{p}_0 perfectly match the exact initial stress profiles p_0 .

4.2. Poisson based forward and Volterra inverse solution

While the above computation and inversion of OA signals were performed using solvers, both derived within the framework of the OA Volterra integral equation, we subsequently consider the independent forward solver “SONOS” [28], detailed in subsection 3.1.1. It yields synthetic input data based on the solution of the full wave equation and, bearing in mind that the inversion is accomplished in the paraxial approximation, consequently helps to prevent inverse crime. Note that, since the paraxial approximation on which the OA Volterra integral equation is based describes the underlying wave equation best at sufficiently large distances $|z_D|$, we first focus on the inversion of signals in the acoustic FF. An exemplary inversion procedure considering the Poisson based forward solver and Volterra based inverse solver at $z_D = -1.0$ cm ($D = 8.33$) is shown in Fig. 5. As evident from the figure, the initial acoustic stress profile p_0 features sharp edges at the boundary of the absorbing layer whereas the inverse estimate \tilde{p}_0 is more gently inclined. This is due to the temporal average over a time interval $\Delta t = 0.005$ cm/ c which is used to mimic the finite extension of a detector in an experimental setting (see discussion in section 3.1.1 and Ref. [26]).

To assess the accuracy as well as the limits of the paraxial approximation upon increasing $|z_D|$, we simulated OA signals at various points in the range $z_D = -0.05, \dots, -2.0$ cm. As pointed out in section 3.1.1, the Poisson integral based forward solver yields an OA signal up to an amplitude factor. Hence, in order to be able to quantitatively compare the Volterra based reconstruction \tilde{p}_0 to the true

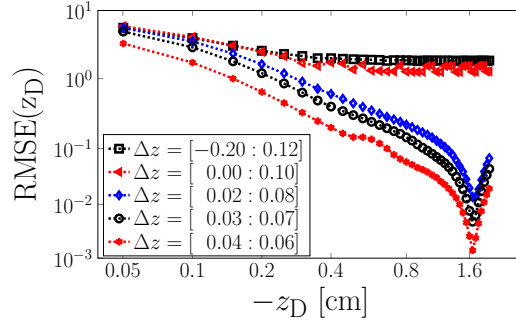


Figure 6. Root mean squared error (RMSE) between the true initial stress profile p_0 and the inverse estimate \tilde{p}_0 for increasingly narrow intervals $\Delta z \equiv [c\tau_- : c\tau_+]$ along the z - and τ -axis, respectively. Note that, in a preprocessing step, p_0 was normalized and \tilde{p}_0 amplitude-adjusted as detailed in the text.

underlying p_0 , we need to adjust the respective signal amplitudes. Therefore, in a preprocessing step we first normalized the initial stress profile so that $\int p_0(\tau) d\tau \equiv 1$ and subsequently adjusted the amplitude of $\tilde{p}_0(\tau)$ so that the residual sum of squares $\text{RSS}(\Delta\tau) = \sum_i^{M(\Delta\tau)} [p_0(\tau_i) - \tilde{p}_0(\tau_i)]^2$ is minimized within the tuning-interval $\Delta\tau = [\tau_- : \tau_+]$ containing $M(\Delta\tau)$ sampling points. The resulting root-mean-square error $\text{RMSE}(\Delta\tau) = \sqrt{\text{RSS}(\Delta\tau)/M(\Delta\tau)}$ as function of the detector-to-layer distance $|z_D|$ is shown in Fig. 6. As evident from the figure, if the tuning interval encloses the region around the signal edges where the reconstructed stress profile is gently inclined, see the curve corresponding to $\Delta z \equiv c\Delta\tau = [-0.02 : 0.12]$ in Fig. 6, the RMSE above $-z_D \approx 0.2$ cm saturates at a finite value characterizing the signal mismatch around the edges. In contrast, if the tuning interval is chosen to be more narrow and to exclude those edge-mismatches, e.g. in the range $\Delta z = [0.02 : 0.08]$, the RMSE decreases as $\propto |z_D|^{-3/2}$ until a limiting point at $z_D \approx -1.5$ cm is reached. This limiting point is solely due to the mesh-width used to discretize the z -axis. Here, we considered a mesh width of $dz = 2.5 \mu\text{m}$. Note that a smaller width dz would in turn allow to shift the limiting point to larger values of $|z_D|$ and to obtain highly precise reconstructed stress profiles also in the deep FF.

4.3. Inversion via successive approximations

An exemplary inversion of an OA signal, obtained using the Poisson integral based forward solver in the acoustic FF at $z_D = -1$ cm, via the Picard-Lindelöf iteration scheme is illustrated in Fig. 7. Therein, the iteration procedure was started off from a low level predictor with $p_0^{(0)}(\tau) = 0$. As evident from Fig. 7(a), the intermediate auxiliary stress profiles $p_0^{(n)}(\tau)$ approach the true initial stress $p_0(\tau)$ upon iteration, featuring a pronounced rarefaction dip that shifts towards larger values of $c\tau$ for increasing n . The convergence of the iteration scheme for the above OA signal is illustrated in Fig. 7(b), where the evolution of the Chebychev-norm $c_n \equiv \|p_0^{(n+1)} - p_0^{(n)}\|$ is shown. The iteration procedure was terminated as soon as the latter decreased below the threshold $c_n \leq 10^{-6}$.

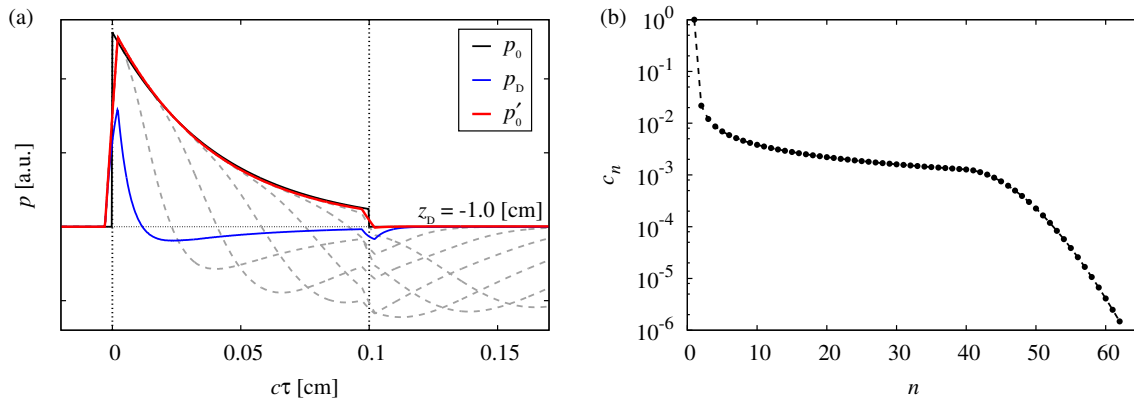


Figure 7. (Color online) Solution of the source reconstruction problem using a Picard-Lindelöf iteration scheme for synthetic input data, starting off from the low level predictor $p_0^{(0)}(\tau) = 0$. (a) Inversion of an OA signal p_D , computed for the detection point $z_D = -1$ cm (solid black solid line), to an initial stress profile p'_0 (solid gray line). As evident from the figure, the inverted signal compares well to the initial acoustic stress profile p_0 . The intermediate auxiliary stress profiles (dashed gray lines; referring to $n = 5, 10, 15, 20, 25$ and 30 iteration cycles) feature a pronounced rarefaction dip that shifts towards larger values of $c\tau$ upon iteration. (b) Illustration of the convergence of the iteration scheme. The iteration procedure is stopped as soon as the Chebyshev-norm between two subsequent profiles decreases below $c_n \equiv \|p_0^{(n+1)} - p_0^{(n)}\| < 10^{-6}$. The final predictor is thus $p'_0 = p_0^{(n=62)}$.

The flattening of the c_n curve in the range $n = 10$ through 40 iterations is mainly due to the pronounced rarefaction phase featured by the auxiliary stress profiles. As soon as the latter shifts beyond $c\tau = 0.20$ cm, i.e. the boundary of the computational domain used in our simulation, the value of c_n continues to decrease noticeably, approaching the final predictor $p'_0 = p_0^{(n=62)}$.

5. Summary

In the presented article, we discussed OA signal generation in the paraxial approximation to the full wave equation. We introduced and detailed numerical schemes to simulate OA signals in the forward direction, where we considered a Poisson integral based solver for the forward direction and a Volterra integral based solver for the paraxial approximation. Further, regarding the inverse OA problem, we considered solvers based on the OA Volterra integral, only.

By means of numerical experiments, geared towards actual laboratory experiments for existing polyvinyl alcohol hydrogel (PVA-H) based tissue phantoms reported in Ref. [26] we characterized OA signals in the acoustic near- and far-field in the paraxial approximation in the forward and inverse direction. Further, in the far-field, where the particular theoretical model can be expected to approximate the full OA wave equation well, we accomplished the inversion of OA signals to initial stress profiles resulting from input obtained by solving the direct problem for the full OA wave equation. Thus,

even if the signal is not produced by the Volterra integral itself, the initial absorption profile can nevertheless be reconstructed using the developed numerical procedure and, material characteristics, as, e.g., the thickness of absorbing layers can be determined reliably. We further assessed the quantitative agreement between the reconstructed and true initial stress profiles as one proceeds towards the far-field. This regime is of particular interest since it allows for OA depth profiling for absorbing structures. This is of pivotal relevance for various applications that strive to reconstruct internal material properties on the basis of external OA signal measurements.

Finally, from a point of view of computational theoretical physics, we presented a self-contained numerical approach to the solution of the source reconstruction problem in the field of inverse optoacoustics. Albeit there exist several general schemes for the forward and inverse solution of the underlying Volterra equation, this particular inverse problem for the paraxial approximation of the OA wave equation has not yet received much attention in the literature. Here, capitalizing on the particular structure of the Volterra operator, i.e. the diffraction-term in the optoacoustic Volterra integral equation, we could derive highly (time-)efficient numerical forward and inverse solvers, thus presenting a methodological progress in the field of optoacoustics.

It is now intriguing to conjecture a further inverse problem related to the OA Volterra integral equation, that is, the Volterra kernel reconstruction problem. It aims at effectively modeling the diffraction transformation of OA signals based on the knowledge of initial stress profiles and detected OA signals, and is not satisfactorily solved in the literature, yet. Such investigations are underway in our group.

Acknowledgments

We thank E. Blumenröther for valuable discussions and comments, as well as for critically reading the manuscript. J. S. acknowledges support from the German Federal Ministry of Education and Research (BMBF) in the framework of the project MeDiOO (Grant FKZ 03V0826). O. M. acknowledges support from the VolkswagenStiftung within the “Niedersächsisches Vorab” program in the framework of the project “Hybrid Numerical Optics - HYMNOS” (Grant ZN 3061). Further valuable discussions within the collaboration of projects MeDiOO and HYMNOS at HOT are gratefully acknowledged.

References

- [1] P. Kuchment and L. Kunyansky. Mathematics of thermoacoustic tomography. *European Journal of Applied Mathematics*, 19:191–224, 2008.
- [2] L.V. Wang. *Photoacoustic Imaging and Spectroscopy*. Optical Science and Engineering. CRC Press, 2009.
- [3] D. Colton and R. Kress. *Inverse Acoustic and Electromagnetic Scattering Theory (Third Edition)*. Springer, 2013.
- [4] V. E. Gusev and A. A. Karabutov. *Laser Optoacoustics*. American Institute of Physics, 1993.
- [5] L. D. Landau and E. M. Lifshitz. *Fluid Mechanics (Second Edition)*. Pergamon, 1987.

- [6] I. Stoffels, S. Morscher, I. Helfrich, U. Hillen, J. Leyh, N. C. Burton, T. C. P. Sardella, J. Claussen, T. D. Poeppel, H. S. Bachmann, A. Roesch, K. Griewank, D. Schadendorf, M. Gunzer, and J. Klode. Metastatic status of sentinel lymph nodes in melanoma determined noninvasively with multispectral optoacoustic imaging. *Science Translational Medicine*, 7(317):317ra199, 2015.
- [7] I. Stoffels, S. Morscher, I. Helfrich, U. Hillen, J. Leyh, N. C. Burton, T. C. P. Sardella, J. Claussen, T. D. Poeppel, H. S. Bachmann, A. Roesch, K. Griewank, D. Schadendorf, M. Gunzer, and J. Klode. Erratum for the research article: “metastatic status of sentinel lymph nodes in melanoma determined noninvasively with multispectral optoacoustic imaging” by i. stoffels, s. morscher, i. helfrich, u. hillen, j. lehy, n. c. burton, t. c. p. sardella, j. c. . . . *Science Translational Medicine*, 7(319):319er8, 2015.
- [8] M. Xu and L. V. Wang. Universal back-projection algorithm for photoacoustic computed tomography. *Phys. Rev. E*, 71(1):016706, 2005.
- [9] K. P. Köstli, D. Frauchiger, J. J. Niederhauser, G. Paltauf, H. P. Weber, and M. Frenz. Optoacoustic imaging using a three-dimensional reconstruction algorithm. *Selected Topics in Quantum Electronics, IEEE Journal of*, 7(6):918–923, 2001.
- [10] Y. Xu and L. V. Wang. Time reversal and its application to tomography with diffracting sources. *Phys. Rev. Lett.*, 92:033902, 2004.
- [11] P. Burgholzer, G. J. Matt, M. Haltmeier, and G. Paltauf. Exact and approximative imaging methods for photoacoustic tomography using an arbitrary detection surface. *Phys. Rev. E*, 75:046706, 2007.
- [12] G. Paltauf, J. A. Viator, S. A. Prahl, and S. L. Jacques. Iterative reconstruction algorithm for optoacoustic imaging. *J. Acoust. Soc. Am.*, 112(4):1536–1544, 2002.
- [13] X. L. Deán-Ben, A. Buehler, V. Ntziachristos, and D. Razansky. Accurate model-based reconstruction algorithm for three-dimensional optoacoustic tomography. *Medical Imaging, IEEE Transactions on*, 31:1922–1928, 2012.
- [14] Jean Provost and Frédéric Lesage. The application of compressed sensing for photo-acoustic tomography. *Medical Imaging, IEEE Transactions on*, 28(4):585–594, 2009.
- [15] Z. Belhachmi, T. Glatz, and O. Scherzer. A direct method for photoacoustic tomography with inhomogeneous sound speed. *Inverse Problems*, 32(4):045005, 2016.
- [16] A. Karabutov, N. B. Podymova, and V. S. Letokhov. Time-resolved laser optoacoustic tomography of inhomogeneous media. *Appl. Phys. B*, 63:545–563, 1996.
- [17] A. C. Tam. Applications of photoacoustic sensing techniques. *Rev. Mod. Phys.*, 58:381–431, 1986.
- [18] R. A. Kruger, P. Liu, Y. Fang, and C. R. Appledorn. Photoacoustic ultrasound (PAUS) - Reconstruction tomography. *Medical Physics*, 22:1605–1609, 1995.
- [19] Note that Ref. [18] put the heat conduction equation under scrutiny, finding that for pulse durations $t_p < 1 \mu\text{s}$ and absorption lengths $\ell > 1 \text{ mm}$, the rate of temperature change exceeds thermal diffusion in tissue by a factor of already $\approx 10^6$. Here, we might consider absorption lengths of $\ell \approx 1 \text{ mm}$ and pulse durations $t_p \approx 10 \text{ ns}$, thus justifying the thermal confinement approximation in our hypothetical case.
- [20] Note that formally, the temporal delta-function might be represented by a sequence of functions $\delta_{t_p}(t) = (\pi t_p)^{-1/2} \exp(-(t/t_p)^2)$ in the limit $\delta(t) = \lim_{t_p \rightarrow 0} \delta_{t_p}(t)$. If we assume a hypothetical situation with absorption lengths of $\ell \approx 1 \text{ mm}$ and sound velocity $c = 1500 \text{ m/s}$ this yields typical propagation times of $\approx 1 \mu\text{s}$. Thus, pulse durations of $t_p \approx 10 \text{ ns}$ might suffice to approve stress confinement.
- [21] G. Paltauf and H. Schmidt-Kloiber. Pulsed optoacoustic characterization of layered media. *Journal of Applied Physics*, 88:1624–1631, 2000.
- [22] Note that, so as to exclude the nonphysical effect of a point source on itself, the Poisson integral has to be understood in terms of its principal value if the source volume V' contains the field point \vec{r} .
- [23] G. Paltauf and H. Schmidt-Kloiber. Measurement of laser-induced acoustic waves with a calibrated optical transducer. *J. Appl. Phys.*, 82(4):1525–1531, 1997.

- [24] G. Paltauf, H. Schmidt-Kloiber, and M. Frenz. Photoacoustic waves excited in liquids by fiber-transmitted laser pulses. *J. Acoust. Soc. Am.*, 104:890–897, 1998.
- [25] M. Jaeger, J. J. Niederhauser, M. Hejazi, and M. Frenz. Diffraction-free acoustic detection for optoacoustic depth profiling of tissue using an optically transparent polyvinylidene fluoride pressure transducer operated in backward and forward mode. *Journal of Biomedical Optics*, 10(2):024035, 2005.
- [26] E. Blumenröther, O. Melchert, M. Wollweber, and B. Roth. Detection, numerical simulation and approximate inversion of optoacoustic signals generated in multi-layered PVA hydrogel based tissue phantoms, 2016. arXiv:1605.05657 (unpublished).
- [27] Also referred to as the paraxial approximation.
- [28] A Python implementation of our code for the solution of the photoacoustic Poisson equation in cylindrical polar coordinates, can be found at Ref. [37].
- [29] W.H. Press, B.P. Flannery, S.A. Teukolsky, and W.T. Vetterling. *Numerical Recipes in FORTRAN 77*. Numerical Recipes in FORTRAN: The Art of Scientific Computing. Cambridge University Press, 1992.
- [30] M. Hazewinkel. *Encyclopaedia of Mathematics*. Encyclopaedia of Mathematics: An Updated and Annotated Translation of the Soviet "Mathematical Encyclopaedia". Springer, 1987.
- [31] D. Michie. Memo Functions and Machine Learning. *Nature*, 218:19–22, 1968.
- [32] M. W. Sigrist. Laser generation of acoustic waves in liquids and gases. *J. Appl. Phys.*, 60:R83–R122, 1986.
- [33] K. Mitsuhashi, K. Wang, and M. A. Anastasio. Investigation of the far-field approximation for modeling a transducer’s spatial impulse response in photoacoustic computed tomography. *Photoacoustics*, 2(1):21–32, 2014.
- [34] E. Hairer, S. P. Nørsett, and G. Wanner. *Solving Ordinary Differential Equations I (2Nd Revised. Ed.): Nonstiff Problems*. Springer-Verlag New York, Inc., New York, NY, USA, 1993.
- [35] Note that such an approach might be considered as committing inverse crime [36], i.e. performing a (putative) trivial inversion of synthetic data obtained by first solving the forward problem in terms of the same exact model. However, here we use this approach as a proof of principle and consider an independent forward solver (with no connection to the Voltarra based solver) in subsequent sections.
- [36] D. Colton and R. Kress. *Inverse acoustic and electromagnetic scattering theory*, volume 93. Springer Science & Business Media, 2012.
- [37] O. Melchert. SONOS – A fast Poisson integral solver for layered homogeneous media. <https://github.com/omelchert/SONOS.git>, 2016.